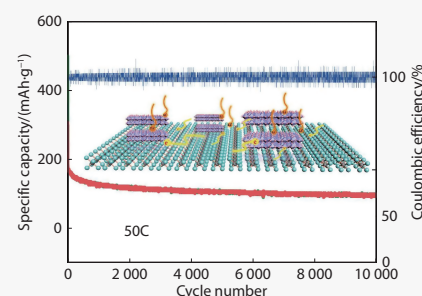


2D Nb₂O₅@2D metallic RuO₂ heterostructures as highly reversible anode materials for lithium-ion batteries

Hai Yang^{1,5}, Fuxiang He^{3,4,5}, Jialong Shen¹, Zhihao Chen¹, Yu Yao¹, Lixin He^{3,4} and Yan Yu^{1,2*} 

Constructing two-dimensional (2D) heterostructured materials by stacking different 2D materials could combine the merits of the individual building blocks while getting rid of the associated shortcomings. Orthorhombic Nb₂O₅ (T-Nb₂O₅) is one of the greatly promising candidates for durable and safety anode for Li-ion batteries (LIBs), but it usually exhibits poor electrochemical performance due to the low electronic conductivity. Herein, we realize excellent lithium storage performance of T-Nb₂O₅ by designing 2D Nb₂O₅@2D metallic RuO₂ heterostructures (Nb₂O₅@RuO₂). The presence of 2D metallic RuO₂ leads to enhanced electronic conductivity. The 2D Nb₂O₅@RuO₂ heterostructures possess very short diffusion length of ions/electrons, easy penetration of liquid electrolyte, and high conductivity transport of electrons through the 2D metallic RuO₂ to 2D Nb₂O₅. The Nb₂O₅@RuO₂ delivers remarkable rate performance (133 mAh g⁻¹ and 106 mAh g⁻¹ at 50 C and 100 C) and excellent long-life capacity (97 mAh g⁻¹ after 10000 cycles at 50 C). Moreover, Nb₂O₅@RuO₂//LiFePO₄ full batteries also display high rate capability of 140 mAh g⁻¹ and 90 mAh g⁻¹ at 20 C and 50 C, respectively. Theoretical calculation results show that the 2D Nb₂O₅@RuO₂ heterostructures possess more large adsorption ability for Li⁺ than that of Nb₂O₅, indicating an excellent lithium storage performance.



Nowadays, the energy crises and environmental pollution resulting from the overdependence of fossil fuels have drawn the worldwide attention. There is an increased demand for developing clean and renewable energy. Lithium-ion batteries (LIBs), as chemically storing energy devices, have been widely applied in portable electronic devices and demonstrated as promising energy storage system for hybrid electric vehicles (HEVs), electric vehicles (EVs), and smart grids.^[1-3] The developments of LIBs with high energy density and high power density rely heavily on the high performance electrode materials. Graphite is the most conventional anode material for LIBs, which possesses a lithiation potential of below 0.2 V (vs. Li⁺/Li).^[4] Such low lithiation potential induce major safety issues due to the electrolytic decomposition and lithium dendrites formation. Further-

more, it displays unsatisfactory capacity at high current density due to its low Li ion diffusion coefficient and the formation of solid electrolyte interphase (SEI) on its surfaces.^[5-8] Typical insertion-type anode materials, such as Li₄Ti₅O₁₂,^[9-10] TiNb₂O₇,^[11-12] orthorhombic Nb₂O₅^[13-15] are investigated extensively because of their better capacity retention than convention- and alloy-type ones. Among them, orthorhombic Nb₂O₅ (T-Nb₂O₅) has shown excellent lithium ions pseudocapacitive in nonaqueous electrolytes since the empty octahedral sites between (001) planes offer natural tunnels for lithium ion transport.^[16] When used for LIBs, the T-Nb₂O₅ shows a suitable voltage range from 1.1 to 2.0 V vs. Li⁺/Li, corresponding to a comparatively high reversible theoretical capacity of about 200 mAh g⁻¹ to form Li_xNb₂O₅ (x = 2).^[13,17-20] Moreover, it can use aluminum foil as the anode current collector rather than expensive and heavy copper foil, because Li does not alloy with aluminum above 0.3 V vs. Li⁺/Li.^[21-22] However, the intrinsic drawback of poor electrical conductivity ($\approx 3 \times 10^{-6}$ S cm⁻¹) and severe pulverization during charge/discharge prevent its practical applications for high performance LIBs.^[23] Considerable attention has been made to enhance the electrochemical performance of T-Nb₂O₅. Construction of nanosized T-Nb₂O₅ (i.e., nanobelts,^[24] vein-like nanoporous networks,^[25] hierarchical microspheres^[26] and nanofibers^[27]) is one of the most effective approach. Another strategy for overcoming low electronic conductivity is to mix Nb₂O₅ with conductive materials such as graphene^[28], carbon nanotubes (CNTs),^[29-30] Graphite^[31]

When used for energy storage system, two-dimensional

¹ Hefei National Research Center for Physical Sciences at the Microscale, Department of Materials Science and Engineering, iChEM (Collaborative Innovation Center of Chemistry for Energy Materials), CAS Key Laboratory of Materials for Energy Conversion, University of Science and Technology of China, Hefei 230026, China

² National Synchrotron Radiation Laboratory, Hefei 230026, China

³ Key Laboratory of Quantum Information University of Science and Technology of China, Hefei 230026, China

⁴ Synergetic Innovation Center of Quantum Information and Quantum Physics, University of Science and Technology of China, Hefei 230026, China

* Corresponding author, E-mail: yanyumse@ustc.edu.cn

Received 20 August 2022; Accepted 27 September 2022; Published online

⁵ These authors contributed equally to this work.

(2D) materials show unprecedented properties that differ from their bulk systems, because the characteristic time constant τ for ion diffusion is proportional to the square of the diffusion length L ($\tau \approx L^2/D$).^[32] Single-crystalline mesoporous T-Nb₂O₅ nanosheets/graphene composites have demonstrated enhanced intercalation/deintercalation characteristics by shortening ions diffusion length and accelerating electron transport.^[33] 2D heterostructured materials, prepared by stacking different 2D crystals on top of each other at the nanoscale, could combine the collective advantages of individual building blocks and synergistic properties. In addition, the 2D heterostructured materials have high specific surface area, enabling improved performances for surface dominant reactions. Gogotsi *et al* reported that MoS₂-on-MXene heterostructures show high performance lithium storage performance.^[34] One can expect that rational design 2D T-Nb₂O₅@2D metallic metal oxide heterostructures could significantly improve its energy storage properties. Among 2D metal oxides, RuO₂ nanosheets are considered to be the most promising metal oxides because of their metal-like electrical conductivity, which exhibits a highly conductive property ($\approx 2 \times 10^4 \text{ S cm}^{-1}$)^[20,35] and fast Li permeation.^[36]

In this work, we designed 2D Nb₂O₅@2D metallic RuO₂ heterostructures (denoted as Nb₂O₅@RuO₂) as anode for high performance LIBs. This unique 2D heterostructures combine a variety of advantages: 1) The intimate interfacial interaction between T-Nb₂O₅ and the metallic RuO₂ can not only facilitate the electron transfer, but also offer high electrode/electrolyte contact surface area for quick electrolyte infiltration, reaching the full potential of the active material (Nb₂O₅). 2) The confined thickness within a nanoscale range of Nb₂O₅@RuO₂ shorten the diffusion length of lithium ions. 3) The Nb₂O₅ nanosheets possess strong interaction with RuO₂ nanosheets, which keeps the structure stability of Nb₂O₅@RuO₂ after repeated Li⁺ intercalation/deintercalation, thus leading to excellent electrochemical performance. When used as anode for LIBs, the Nb₂O₅@RuO₂ can deliver excellent cyclability and rate performance, which demonstrates capacity of 97 mAh g⁻¹ after 10000 cycles at 50 C. Additionally, a full battery has been assembled by using Nb₂O₅@RuO₂ and LiFePO₄ as anode and cathode, respectively. The full battery demonstrates enhanced charge and discharge ability (140 mAh g⁻¹ and 90 mAh g⁻¹ at 20 C and 50 C, respectively). Moreover, theoretical calculations reveal the presence of the RuO₂ layer indeed improves the stability of lithium ions adsorption and reduces the diffusion barrier of lithium ions in the Nb₂O₅.

Materials and methods

Materials synthesis

As reported previously,^[35,37] the KNb₃O₈ and NaRuO₂ were synthesized by calcination of stoichiometric Nb₂O₅ and K₂CO₃ at 900 °C for 10 h in air and Na₂CO₃, Ru and RuO₂ at 900 °C for 12 h in Ar atmosphere, respectively. Protonation was realized by mixed KNb₃O₈ and NaRuO₂ with acid aqueous for one week. In a typical procedure, 1.0 g of KNb₃O₈ and NaRuO₂ were dispersed in 60 mL nitric acid (6 mol L⁻¹) and 500 mL hydrochloric acid (1 mol L⁻¹), respectively. The exfoliation of HNb₃O₈ and HRuO₂ were achieved by intercalation of tet-

ra-butylammonium (TBA) cation into the layer. Note that the TBA⁺/H⁺ = 5. The resultant solution was shaken for two weeks and followed by ultrasonic treatment. Subsequently, the suspensions were centrifuged at 2000 rpm for 30 min to separate the non-exfoliated sediment. The dry TBA-Nb₃O₈ and TBA-RuO₂ were obtained by after centrifugal separation and drying in vacuum freeze drier. The TBA-Nb₃O₈ and TBA-RuO₂ were dissolved in water with mass ratio of 6:1 to form uniform solution by stirring and ultrasonic dispersion. Subsequently, the Nb₂O₅@RuO₂ was obtained by freeze drying. Finally, the precursor was annealing at 600 °C for 2 h in air. The pure Nb₂O₅ nanosheets were obtained by directly heating the TBA-Nb₃O₈ at same condition.

Materials characterization

The morphologies of samples were observed by scanning electron microscopy (CIQTEK SEM3100 and Hitachi, SU8200) and transmission electron microscopy (JEOL, JEM-2100F). The crystalline structure of samples was examined by X-ray diffraction (TTR-III, Rigaku). Bonding states of the atoms were investigated by XPS (Thermo-VG Scientific, ESCALAB 250). Raman spectrum was obtained by a LanRanHR (HORIBA Scientific, Paris, France) spectrometer. Nitrogen adsorption/desorption isotherms were characterized by an ASAP 2020 accelerated surface area and porosimetry system. The thermogravimetric analysis using TGA Q5000 instrument (10 °C/min from 30 to 800 °C in air).

Electrochemical characterization

To prepare the electrodes for 2032 coin cell assembly, the samples were mixed with acetylene black and poly(vinylidene) in a mass ratio of 7:2:1 in an N-methylpyrrolidone solvent. Then the slurry was coated on the copper foil and dried in vacuum oven 60 °C overnight. The cell was assembled in glove box (the water and oxygen concentrations were kept below 0.1 ppm), using Li metal as counter and reference electrode and Celgard 2400 as the separator. The electrolyte was composed of 1 M LiPF₆ dissolved in ethylene carbonate (EC) and dimethyl carbonate (DEC) (1:1, w/w). The CV curves and EIS were obtained on electrochemical workstation (CHI 660D). The charge and discharge were evaluated by battery test system (Neware BTS-610). For the fabrication of Nb₂O₅@RuO₂//LiFePO₄ full cell, the commercial LiFePO₄ electrode was used as cathode and the activated Nb₂O₅@RuO₂ was used as anode. The Nb₂O₅@RuO₂ electrodes used in the full cells were cycled in half cells before they were assembled into full cells. The full cell was fabricated with Nb₂O₅@RuO₂ as the anode and LiFePO₄ as the cathode with a mass ratio of 1:3, the capacity ratio of the negative electrode to positive electrode (N/P ratio) is about 0.67.

Theoretical calculations

The calculations for structure optimization, self-consistent and energy barrier are carried out with the ABACUS package.^[38] The exchange-correlation function is treated by the generalized gradient approximation (GGA) in the form of the Perdew-Burke-Ernzerhof (PBE) functional.^[39] We use the SG15 optimized Norm-Conserving Vanderbilt (ONCV) multiprojector pseudopotentials to describe the electronic potential field of the core.^[40] At the same time, the numerical atomic orbital basis set is expanded using Standard DZP Orbitals. The convergence criterion for electronic self-consistent cal-

culations is $5.0E-7$ eV. Both the atomic positions and the lattice parameters are allowed to change during the structural relaxation until the Hellmann-Feynman forces on each atom are lower than $2.0E-2$ eV/Å. We employ numerically tabulated atom-centered orbitals as the basis functions to expand electronic wave functions. Specifically, we choose the basis sets $4s2p2d1f$ for Ru and Nb elements, $2s2p1d$ for O element and $4s1p$ for Li element. Brillouin-Zone (BZ) integration was sampled by Gamma point in the reciprocal space in order to improve computational efficiency. We take the van der Waals DFT-D3 interaction into account in the calculation of the $Nb_2O_5@RuO_2$ heterojunction system, which makes the simulation results more accurate.^[41]

The establishment of hypothesis model of T- Nb_2O_5 : previous experimental fitting proposed a virtual crystal model of T- Nb_2O_5 ($Nb_{16.8}O_{42}$), but the fraction occupation of Nb or O made DFT calculation expensive. Therefore, we made the following rational approximations to the T- Nb_2O_5 structure

model: (1) A small amount of the amorphous Nb cannot be considered because the location is not defined and stoichiometry is fractioned; (2) Two nearest Nb atoms (the distance is 0.43 Å, occupations are 0.5) are replaced with their average sites (occupations are 1.0) owing to avoid Nb deviating from the equilibrium positions during self-consistent calculations; (3) Two oxygen atoms at the 2b Wyckoff positions are removed from the model to balance the charge of the entire unit cell, and there is no Raman active modes at 2b Wyckoff positions.^[42] Through these approximations, the unit cell of T- Nb_2O_5 shows higher space symmetry than the original $Nb_{16.8}O_{42}$ model and space group is Pbam.

Results and Discussion

The $Nb_2O_5@RuO_2$ heterostructures were obtained as schematically illustrated in Figure 1a. Firstly, layered potassium triniobate (KNb_3O_8) and sodium ruthenate ($NaRuO_2$) were

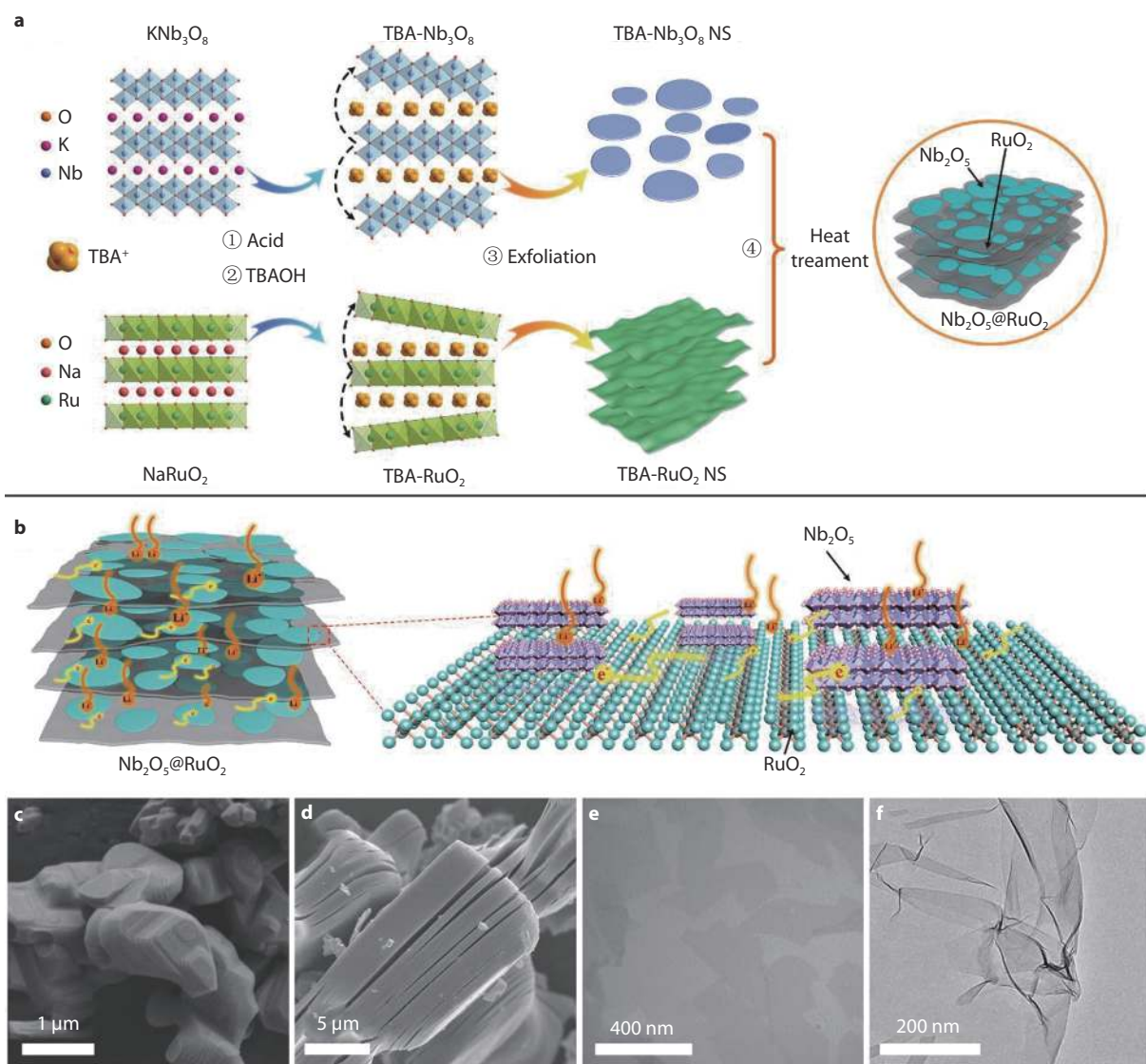


Fig. 1 Schematic illustrations of **a** the synthesis process of $Nb_2O_5@RuO_2$. **b**, The lithium ions and electrons transportation process. SEM images of **c** KNb_3O_8 and **d** $NaRuO_2$. TEM images of **e** TBA- Nb_3O_8 and **f** TBA- RuO_2 .

fabricated *via* solid-state reaction. Subsequently, layered protonic triniobate (HNb_3O_8) and ruthenate (HRuO_2) were obtained by proton-exchange reaction with acid solution. The exfoliation of layered HNb_3O_8 and HRuO_2 were achieved by the intercalation of tetrabutylammonium (TBA) cation and followed by ultrasonic treatment, the exfoliated nanosheets (NSs) labeled as TBA- Nb_3O_8 NSs and TBA- RuO_2 NSs, respectively. Finally, TBA- Nb_3O_8 NSs and TBA- RuO_2 NSs were mixed and annealed treatment in air to convert precursors into $\text{Nb}_2\text{O}_5@/\text{RuO}_2$ heterostructures. As shown in Figure 1b, the $\text{Nb}_2\text{O}_5@/\text{RuO}_2$ heterostructures feature intimate interfacial interactions, which maximize the potential of conductive RuO_2 as support for Nb_2O_5 . The ultrathin heterostructures significantly shortens the electrons/ions diffusion length, resulting in excellent rate capability.

Scanning electron microscopy (SEM) and transmission electron microscopy (TEM) were employed to observe the morphology and microstructure of the precursors, intermediate products and final products. Both the SEM images of KNb_3O_8 and NaRuO_2 display obvious stacked layer structure (Figure 1c & 1d). The particle size of NaRuO_2 (few dozen micrometers) is

bigger than that of KNb_3O_8 (several micrometers). After chemical exfoliation by TBA, KNb_3O_8 and NaRuO_2 are transferred to TBA- Nb_3O_8 (Figure S1a) and TBA- RuO_2 (Figure S1b), respectively, realizing 2D nanostructures with well-defined morphology. The ultrathin morphologies of the TBA- Nb_3O_8 (Figure 1e) and TBA- RuO_2 (Figure 1f) are confirmed by TEM. The width of TBA- Nb_3O_8 NSs and TBA- RuO_2 NSs are approximately 200-500 nm and several micrometers, respectively. The X-ray diffraction (XRD) patterns of TBA- Nb_3O_8 and TBA- RuO_2 are displayed in Figure S2 and S3, exhibiting the characteristic peaks of the exfoliated nanosheets.^[35,37]

Figure 2a & 2b clearly exhibit 2D nanosheets morphology of $\text{Nb}_2\text{O}_5@/\text{RuO}_2$ with the size of about 2-10 μm . Figure 2c & 2d further confirm ultrathin 2D nanosheets of $\text{Nb}_2\text{O}_5@/\text{RuO}_2$ heterostructures, which maintains similar structure with precursors. The high-resolution transmission electron microscopy (HRTEM) images are revealed in Figure 2e & 2f and Figure S4. Figure 2e shows the visible lattice fringes with a lattice spacing of 0.39 \AA , which are consistent with the (001) plane of T- Nb_2O_5 .^[43] Figure 2f and Figure S4 reveal the Nb_2O_5 and RuO_2 are twinborn on one nanosheet with a distinct in-

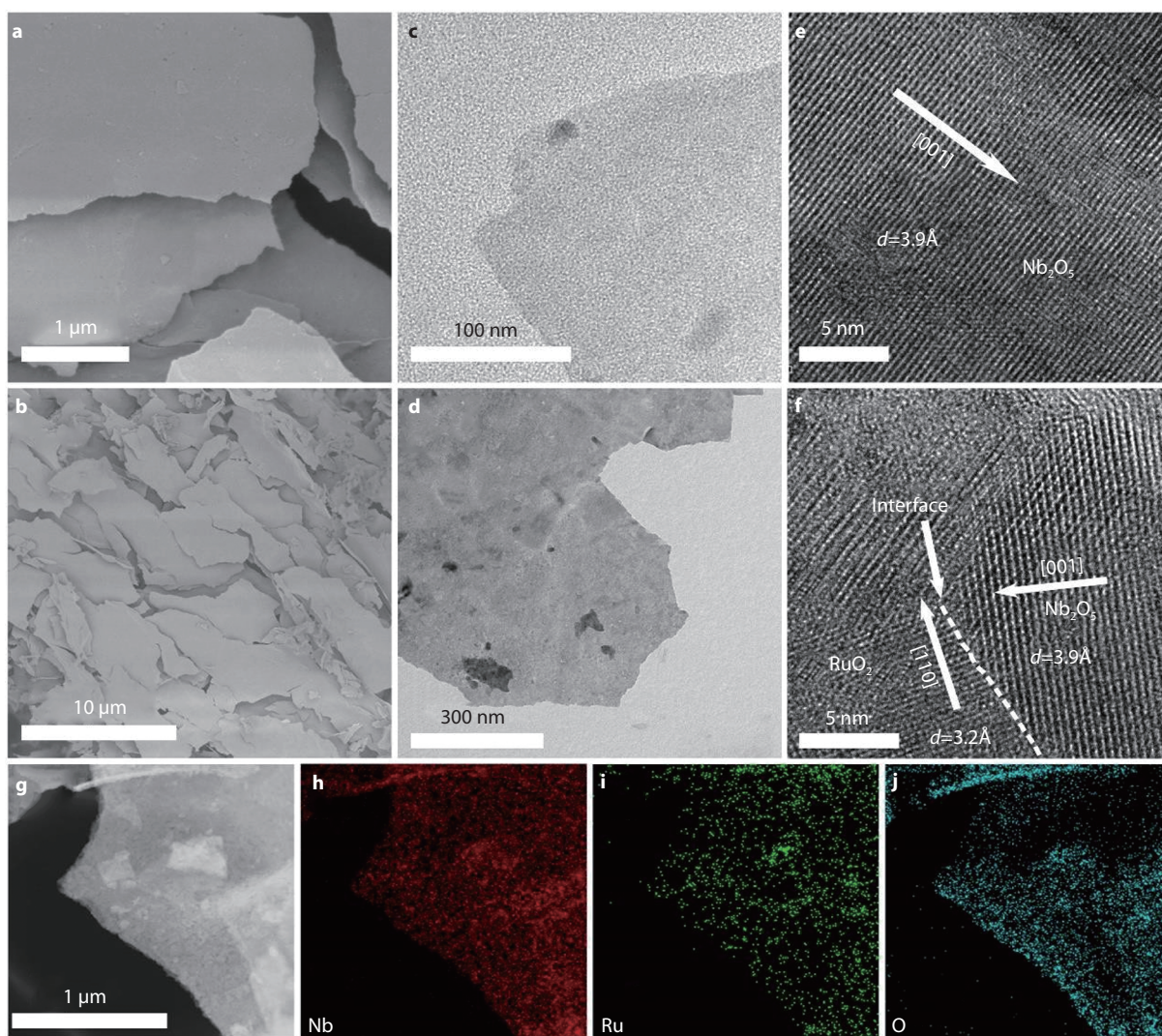


Fig. 2 a, b SEM, c, d TEM, e, f HRTEM, g HADDF-STEM images and corresponding h Nb, i Ru and j O elemental mapping of $\text{Nb}_2\text{O}_5@/\text{RuO}_2$.

interface, forming $\text{Nb}_2\text{O}_5/\text{RuO}_2$ heterostructures. The d -spacing value is measured to be 2.5 Å and 3.9 Å, corresponding to the (101) plane of RuO_2 and (001) plane of $\text{T-Nb}_2\text{O}_5$, respectively.^[44–45] The high angle annular dark-field scanning transmission electron microscopy (HAADF-STEM) and related energy dispersive X-ray spectrometry (EDS) elemental mapping (Figure 2g–2j) prove the Nb_2O_5 and RuO_2 NSs disperse uniformly in the $\text{Nb}_2\text{O}_5/\text{RuO}_2$ heterostructures.

The crystalline phase of Nb_2O_5 , RuO_2 and $\text{Nb}_2\text{O}_5/\text{RuO}_2$ were studied by XRD (Figure S5a). The XRD patterns of Nb_2O_5 and RuO_2 exhibit the standard patterns of Nb_2O_5 (JCPDS No. 30-0873)^[45–46] and RuO_2 (JCPDS No. 40-1290),^[47] respectively. The XRD pattern of $\text{Nb}_2\text{O}_5/\text{RuO}_2$ heterostructures confirms that its composition contains both Nb_2O_5 and RuO_2 . The construction of the $\text{Nb}_2\text{O}_5/\text{RuO}_2$ heterostructure reduces the particle size and crystallinity of RuO_2 , which leads to weaker intensity and larger half width of the diffraction peak.^[48–49] Figure S5b displays the Raman spectra of Nb_2O_5 , RuO_2 and $\text{Nb}_2\text{O}_5/\text{RuO}_2$. The RuO_2 shows three distinct peaks located at 523, 643 and 713 cm^{-1} .^[50–51] And the Nb_2O_5 exhibits four clearly peaks located at 126, 239, 687 and 990 cm^{-1} .^[52] In the case of the $\text{Nb}_2\text{O}_5/\text{RuO}_2$, distinct peaks with those of the RuO_2 and Nb_2O_5 confirm the formation of heterostructures. Figure S6 reveals the X-ray photoelectron spectroscopy (XPS) spectrum of $\text{Nb}_2\text{O}_5/\text{RuO}_2$, the typical shape peaks of Nb 4s, Nb 4p, Nb 3s, Nb 3p, Ru 3p, Ru 3d and O 1s species can be clearly observed in XPS survey spectrum, which demonstrates that the $\text{Nb}_2\text{O}_5/\text{RuO}_2$ includes Nb, Ru and O elements. The high-resolution XPS spectrum can analyze the chemical environment of every element in composites. According to the high-resolution Nb 3d XPS spectrum (Figure S7a), two remarkable peaks located at about 209.9 and 207.1 eV, analogous to Nb 3d_{3/2} and Nb 3d_{5/2}, respectively.^[33,53] As for the high-resolution of Ru 3d (Figure S7b), the binding energies of about 284.8 and 280.6 eV match with Ru 3d_{3/2} and Ru 3d_{5/2}, respectively.^[54–55] Compared with the pure Nb_2O_5 power, the peaks of Nb 3d exhibit slight shift to high bonding energy, demonstrating the enhanced valence state of Nb. Meanwhile, the peaks of Ru 3d display obvious shift to low bonding energy, revealing the decreased Ru valence state. The XPS results confirm that the Nb_2O_5 NSs possess strong interaction with RuO_2 nanosheets instead of simple physical blending, which is in good agreement with the results of HRTEM (Figure 2f).^[54] The chemical bonding of Nb_2O_5 NSs on RuO_2 NSs could maintain the stable structure after long cycles and the metallic RuO_2 NSs work as a cushion to buffer the volume change of Nb_2O_5 during lithiation/delithiation. The nitrogen absorption-desorption technique showed that $\text{Nb}_2\text{O}_5/\text{RuO}_2$ possessed the Brunauer-Emmett-Teller (BET) specific surface area of 30.8 $\text{m}^2 \text{g}^{-1}$ and pore size distribution of 0.7, 1.5, 4 nm, revealing the microporous and mesoporous structure of the hybrid material (Figure S8). The thermogravimetric analysis (TGA) was conducted to check the weight ratio of Nb_2O_5 in $\text{Nb}_2\text{O}_5/\text{RuO}_2$. The content of the RuO_2 and the Nb_2O_5 are about 17 wt.% and 83 wt.%, respectively (Figure S9a & b).

The electrochemical behavior of $\text{Nb}_2\text{O}_5/\text{RuO}_2$ as anode material for LIBs was evaluated in 2032 coin-type cell. Figure 3a displays the first four cyclic voltammetry (CV) curves of $\text{Nb}_2\text{O}_5/\text{RuO}_2$ at a scan rate of 0.1 mV s^{-1} between a voltage window of 1.1–3.0 V (vs. Li^+/Li). During the first Li^+ insertion

process, two reduction peaks located at 1.83 V and 1.5 V were observed, which is attributed to the redox reaction of Nb_2O_5 ($\text{Nb}_2\text{O}_5 + x \text{Li}^+ + x \text{e}^- = \text{Li}_x\text{Nb}_2\text{O}_5$), accompanied by a little decomposition of electrolyte and formation of stable solid electrolyte interphase (SEI) layer.^[56–57] The oxidation peaks were observed at around 1.75 V and 1.93 V during charge process, corresponding to the oxidation of Nb from Nb^{4+} to Nb^{5+} .^[57–58] The CV curves almost overlap after the first cycle, revealing good reversibility after the initial capacity loss. The first three galvanostatic charge/discharge curves of $\text{Nb}_2\text{O}_5/\text{RuO}_2$ are shown in Figure 3b. The $\text{Nb}_2\text{O}_5/\text{RuO}_2$ delivers a reversible charge capacity about 285 mAh g^{-1} at 1 C (1 C = 200 mA g^{-1}), with an initial Coulombic efficiency (ICE) of 61.4%. The initial irreversibility may result from the SEI formation and irreversible Li^+ insert into Nb_2O_5 and RuO_2 .^[17] The typical charge/discharge profiles of RuO_2 were shown in Figure S10, the RuO_2 reacts with Li *via* conversation mechanism in the voltage window below 1.1 V. Thus, the capacity of $\text{Nb}_2\text{O}_5/\text{RuO}_2$ can be mainly attributed to the insertion reaction between lithium ion and Nb_2O_5 . The cycling stability of the $\text{Nb}_2\text{O}_5/\text{RuO}_2$ and the Nb_2O_5 at 5 C are shown in Figure 3c. Obviously, the $\text{Nb}_2\text{O}_5/\text{RuO}_2$ shows higher reversible capacity (165 mAh g^{-1} after 1000 cycles) than that of the Nb_2O_5 (129 mAh g^{-1} after 1000 cycles). The capacity decay of the $\text{Nb}_2\text{O}_5/\text{RuO}_2$ (Figure 3c) was very slow, only 0.03% decay per cycle after the first three cycles at 1 C. The $\text{Nb}_2\text{O}_5/\text{RuO}_2$ not only displays excellent cyclability at a low current density but also shows stable cycle life under a high current density. The SEM images of $\text{Nb}_2\text{O}_5/\text{RuO}_2$ for LIBs after 100 cycles at rate of 5 C is shown in Figure S11, it can still well maintain the 2D morphology. Figure 3d shows the cycling performance of the $\text{Nb}_2\text{O}_5/\text{RuO}_2$ electrode at 50 C. After the initial capacity loss, the Coulombic efficiency reaches $\approx 100\%$. It delivers extraordinary long-life stability of around 97 mAh g^{-1} at 50 C after 10000 cycles, which is higher than that of other Nb_2O_5 -based anode for LIBs (Table S1).

Figure 3e compares the rate performance of the $\text{Nb}_2\text{O}_5/\text{RuO}_2$ and the Nb_2O_5 NSs from 1 C to 100 C. The $\text{Nb}_2\text{O}_5/\text{RuO}_2$ electrode displays excellent rate capability and can be reversibly cycled at 100 C. The $\text{Nb}_2\text{O}_5/\text{RuO}_2$ delivers reversible capacities of 280, 251, 222, 197, 170, 133 and 106 mAh g^{-1} at 1, 2, 5, 10, 20, 50 and 100 C, respectively. In the case of Nb_2O_5 NSs electrode, at the same rate, it can only display low capacities of 186, 176, 160, 145, 124, 97 and 70 mAh g^{-1} , respectively. The enhanced lithium storage properties of the $\text{Nb}_2\text{O}_5/\text{RuO}_2$ heterostructures in comparison to Nb_2O_5 NSs may be attributed to its intimate interfacial interaction between $\text{T-Nb}_2\text{O}_5$ and the metallic RuO_2 , leading to better ionic and electronic conduction throughout the electrode. To get the evidence of enhanced conductivity Nb_2O_5 NSs after introduction of the RuO_2 , the electrochemical impedance spectroscopy (EIS) was carried out to test the both cells after 3 cycles at 1 C (Figure S12). The charge transfer resistance (R_{ct}) of $\text{Nb}_2\text{O}_5/\text{RuO}_2$ (60 Ω) shows more significant decrease than that of Nb_2O_5 (340 Ω), indicating the existence of RuO_2 may be beneficial to reduce polarization. The rate performance of $\text{Nb}_2\text{O}_5/\text{RuO}_2$ is superior to that of other Nb_2O_5 -based anode for LIBs (Figure 3f), such as $\text{Nb}_2\text{O}_5/\text{Nb}_4\text{C}_3\text{T}_x$,^[19] Ag-N- Nb_2O_5 ,^[17] C-T- Nb_2O_5 ,^[58] T- $\text{Nb}_2\text{O}_5/\text{C}$,^[45] Wired-H- Nb_2O_5 ,^[59] Nanoporous Nb_2O_5 ,^[25] $\text{Nb}_2\text{O}_5/\text{HGF}$,^[18] 3D/CNW-T- Nb_2O_5 ,^[60]

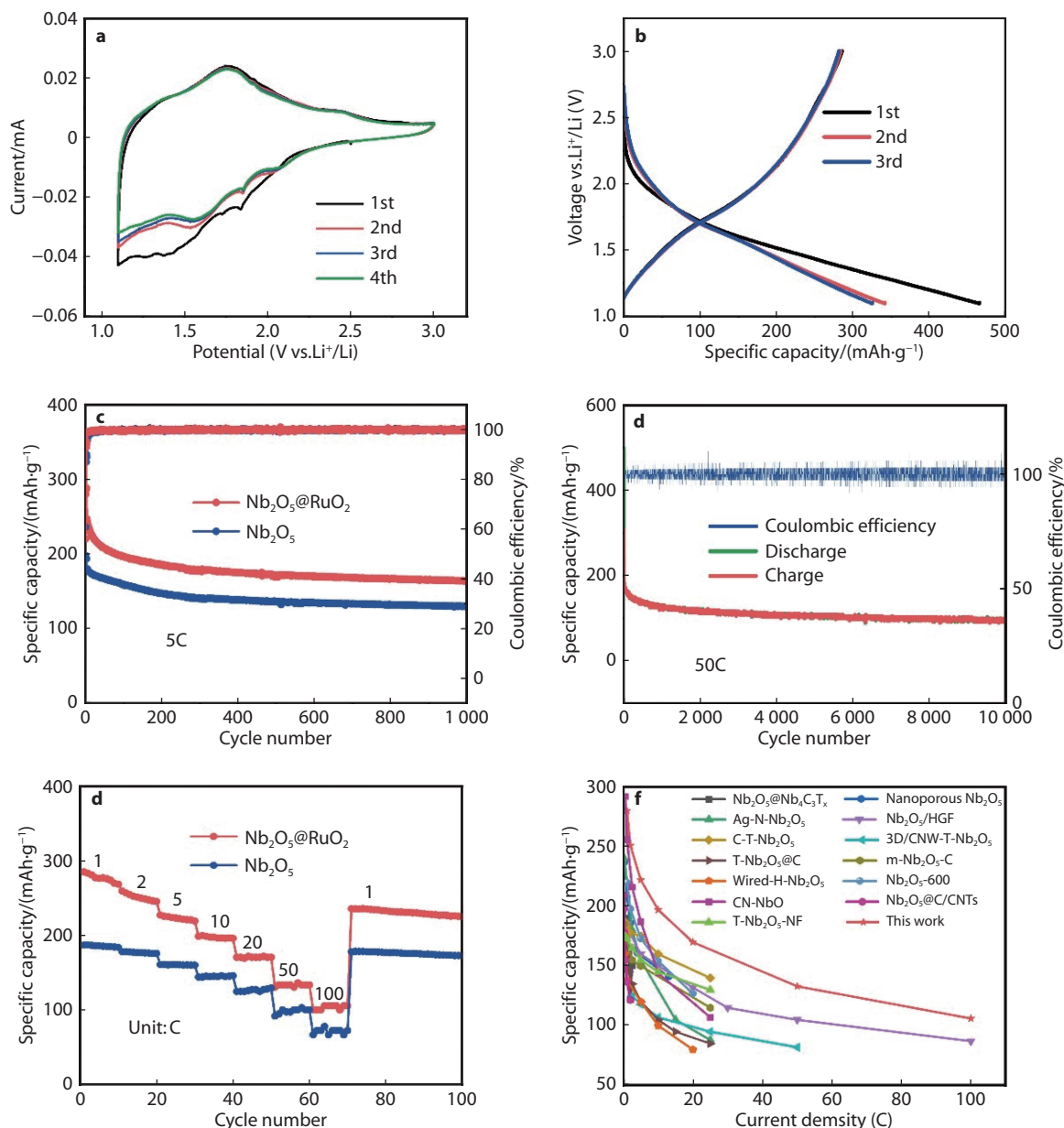


Fig. 3 **a**, CV curves for first four cycles at a scan rate of 0.1 mV s^{-1} . **b**, Galvanostatic charge/discharge curves for first three cycles at 1 C. **c**, Cycling stability at 5 C. **d**, Long-term cycling stability at 50 C of $\text{Nb}_2\text{O}_5@RuO_2$. **e**, Rate capacity at different rates as indicated of $\text{Nb}_2\text{O}_5@RuO_2$ and Nb_2O_5 . **f**, A comparison of rate performance of $\text{Nb}_2\text{O}_5@RuO_2$ with some other reported Nb_2O_5 anode materials.

$m\text{-Nb}_2\text{O}_5\text{-C}$,^[61] $\text{Nb}_2\text{O}_5\text{-600}$,^[62] CN-NbO ,^[14] $\text{Nb}_2\text{O}_5@C/CNTs$,^[30] and $\text{T-Nb}_2\text{O}_5\text{-NF}$.^[15]

It has been demonstrated that a pseudocapacitive mechanism appears when lithium ions are inserted into $\text{T-Nb}_2\text{O}_5$.^[63] To obtain the kinetics information of $\text{Nb}_2\text{O}_5@RuO_2$, CV tests were performed to study the electrochemical behavior of $\text{Nb}_2\text{O}_5@RuO_2$ at different sweep rates from 0.1 to 10 mV s^{-1} (Figure 4a). We plotted the curves of $\log(i)$ versus $\log(v)$ for both oxidation and reduction peak current, where i is current (mA) and v is the sweep rate (mV s^{-1}). As displayed in the Figure 4b, the two parameters (i , v) obey a function relationship as follow^[13,64]:

$$i = av^b \quad (1)$$

$$\log(i) = \log(a) + b\log(v) \quad (2)$$

Where a and b are two parameters of value from 0.5 to 1. It was agreed that $b = 0.5$ reveals a diffusion-controlled process resulted from Li^+ intercalation, and $b = 1$ implies a capacitive process by surface charge storage mechanism.^[65–66] In Figure 4b, the b value calculated from cathodic and anodic peaks are 0.88 and 0.96, respectively, exhibiting the pseudocapacitive behavior of $\text{Nb}_2\text{O}_5@RuO_2$. It can explain why $\text{Nb}_2\text{O}_5@RuO_2$ achieved extraordinary rate performance. The current can be described as a sum of two parts at every potential value, which are capacitive contribution (av) and diffusion-limited contribution ($av^{1/2}$). Therefore, it can be written as follow:

$$i = k_1v + k_2v^{1/2} \quad (3)$$

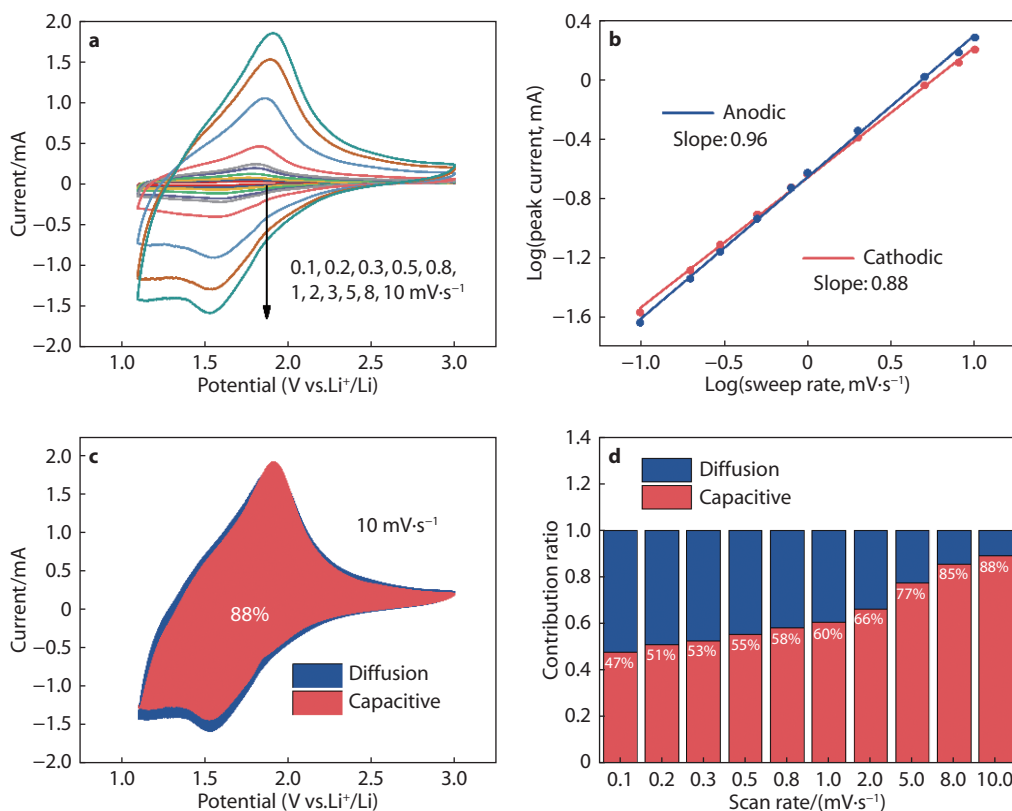


Fig. 4 **a**, CV curves of Nb₂O₅@RuO₂ at various scan rates. **b**, Relationship between the peak currents and scan rates in logarithmic format. **c**, Capacitive contribution of Nb₂O₅@RuO₂ at a scan rate of 10 mV s⁻¹. **d**, Contribution ratio of the capacitive and diffusion-controlled capacity versus scan rate.

$$i/v^{1/2} = k_1 v^{1/2} + k_2 \quad (4)$$

Where k_1 and k_2 are two parameters, which can be easily work out according to Equation (4). According to the integral area of the CV curve, the contribution of capacitance is about 88% of the total charge storage (Figure 4c) at scan rate of 10 mV s⁻¹. The contribution ratios of capacitive and diffusion-controlled at different sweep rates have been calculated as shown in Figure 4d. The percentage of capacitive contribution continuously increases with the increases of sweep rate.

To further demonstrate the possibility of practical application, lithium-ion full cells were assembled by using commercial LiFePO₄ (LFP) as cathode and activated Nb₂O₅@RuO₂ as anode between 1.0 and 3.0 V, as the schematic illustration in Figure 5a.^[67–68] The XRD pattern and SEM image of LFP are shown in Figure S13 and Figure S14, respectively. The morphology of LFP is near-spherical with size of 1–10 μm. The typical charge/discharge curves of LFP half cell ranging from 2.2–4.0 V indicate a plateau around 3.4 V with a discharge capacity of 150 mAh g⁻¹ at 1 C (Figure S15). The LiFePO₄ electrode delivers the capacities of 158, 154, 150, 142, 125, 103, and 70 mAh g⁻¹ at 0.2, 0.5, 1, 2, 5, 10, and 20 C, respectively (Figure S16). Figure 5b shows the charge/discharge curves of LFP//Nb₂O₅@RuO₂ full cell at rate of 2 C to 50 C. The full battery delivers a reversible capacity of about 286 mAh g⁻¹ at 2 C with an average voltage plateau at 1.8 V (the specific capacity and current density are based on the weight of anode material). Figure 5c represents the rate capacity of full cell, delivering reversible capacities of 286, 230, 185, 140 and 90 mAh g⁻¹

at 2, 5, 10, 20 and 50 C, respectively. Figure 5d shows the cycle performance of full cell at 20 C. Remarkably, the full battery maintains good cycling stability and exhibits high reversible capacity (82 mAh g⁻¹ after 500 cycles) with Coulombic efficiency nearly reach 100%. The excellent electrochemical performance of the full cell confirms the potential of practical application of the Nb₂O₅@RuO₂.

The density functional theory (DFT) calculations were performed to explain the lithium storage mechanism and ions transport in Nb₂O₅ and Nb₂O₅@RuO₂. The structure of the Nb₂O₅ crystal is obtained after structural optimization. The atomic arrangement along the c-axis direction is formed by the stacking of 4h layers and 4g layers in turn, of which 4h layers become the primary Nb–O bonding layers, while the 4g layers are completely occupied by oxygen atoms (Figure 6a).^[42,69] The larger spatial gap makes the 4g layer an ideal layer for lithium ions adsorption and bonding. Similarly, the structure-optimized Nb₂O₅/RuO₂ heterojunction system is prepared for subsequent theoretical calculations (Figure 6b). We found eight possible lithium ions adsorption sites on the Nb₂O₅ through structure optimization (Figure 6a), and the corresponding adsorption energy values of different adsorption sites (labeled in Figure 6a) range from -3.31 eV to -3.53 eV (Figure 6c and Table S2). Besides, the lithium ions adsorption energy on Nb₂O₅@RuO₂ (labeled in Figure 6b) range from -3.98 to -4.17 eV (Figure 6c and Table S2). The adsorption energies of lithium ions among Nb₂O₅ and Nb₂O₅@RuO₂ are shown in Figure 6c, revealing the introduction of the RuO₂

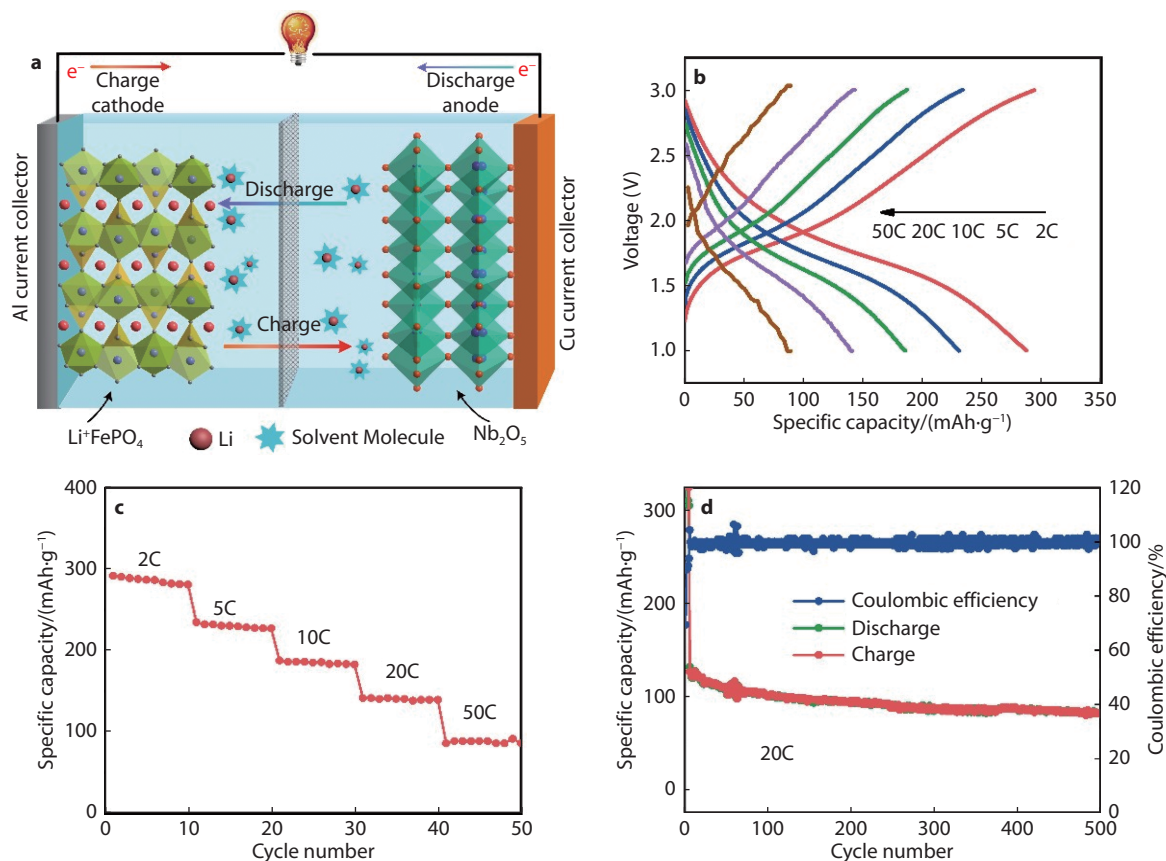


Fig. 5 a, Schematic illustration of the $\text{Nb}_2\text{O}_5/\text{LiFePO}_4$ full cell. b, The charge/discharge curves of full cells at various current densities. c, Rate performance. d, long cycle performance for 500 cycles at 20 C.

layer improves the stability of lithium ions adsorption on the T- Nb_2O_5 4g layer. Then, we simulated the diffusion barrier of lithium ions in the 4g layer along the x-y plane of Nb_2O_5 and $\text{Nb}_2\text{O}_5@/\text{RuO}_2$ using the Climbing Image Nudged Elastic Band (CINEB) method.^[70–71] We simulate the two possible diffusion systems, namely: path 1 is that lithium ions transport from site 4 to another site 4 of the nearest neighbor lattice and path 2 is lithium ions transport path from site 4 to nearest stable site 5 in the same unit cell. The lithium ions diffusivity related migration barriers of Nb_2O_5 along path 1 and path 2 are summarized and compared with those of $\text{Nb}_2\text{O}_5@/\text{RuO}_2$ in Figure 6d and Figure 6e, respectively. The results show that the diffusion of lithium ions in the $\text{Nb}_2\text{O}_5@/\text{RuO}_2$ requires lower energy barriers than those of Nb_2O_5 . In summary, our first-principles calculations show that the presence of the RuO_2 layer indeed improves the stability of lithium ions adsorption and reduces the diffusion barrier of lithium ions in the Nb_2O_5 , which is consistent with the previous experimental results.

Conclusions

In summary, $\text{Nb}_2\text{O}_5@/\text{RuO}_2$ heterostructures have been synthesized via a top-down liquid exfoliation strategy and followed by annealing in air. The intimate interfacial interaction between T- Nb_2O_5 and the metallic RuO_2 combine the collective merits of Nb_2O_5 NSs and RuO_2 NSs and facilitate the syner-

gistic advantages. The metallic RuO_2 can enhance the electronic conductivity of Nb_2O_5 and realize fast Li accessibility. The 2D structure of Nb_2O_5 with high surface can shorten the diffusion path of ions and electrons. The $\text{Nb}_2\text{O}_5@/\text{RuO}_2$ endows remarkable rate performance (133 mAh g^{-1} and 106 mAh g^{-1} at 50 C and 100 C, respectively) and excellent long-life capacity (97 mAh g^{-1} after 10000 cycles at 50 C). The kinetic analysis reveals the pseudocapacitive storage process of $\text{Nb}_2\text{O}_5@/\text{RuO}_2$, which enhances the electrochemistry performance at rapid charge and discharge process. Furthermore, $\text{Nb}_2\text{O}_5@/\text{RuO}_2//\text{LiFePO}_4$ full cell also delivers capacities of 140 mAh g^{-1} and 90 mAh g^{-1} at 20 C and 50 C, respectively, indicating its excellent electrochemical performance. The computation results demonstrate that the strong Li adsorption on the 2D $\text{Nb}_2\text{O}_5@/\text{RuO}_2$ heterostructures leads to its remarkable electrochemical performance. This work paves the way to construct a variety of heterostructures for other applications (i.e., energy storage, catalysis, and sensor).

ACKNOWLEDGEMENTS

This work was supported by the National Natural Science Foundation of China (Nos. 51925207, U1910210, 52161145101, 52102321, and 51872277), the National Synchrotron Radiation Laboratory (KY2060000173), the Joint Fund of the Yulin University and the Dalian National Laboratory for Clean Energy (Grant YLU-DNL Fund 2021002), the Fun-

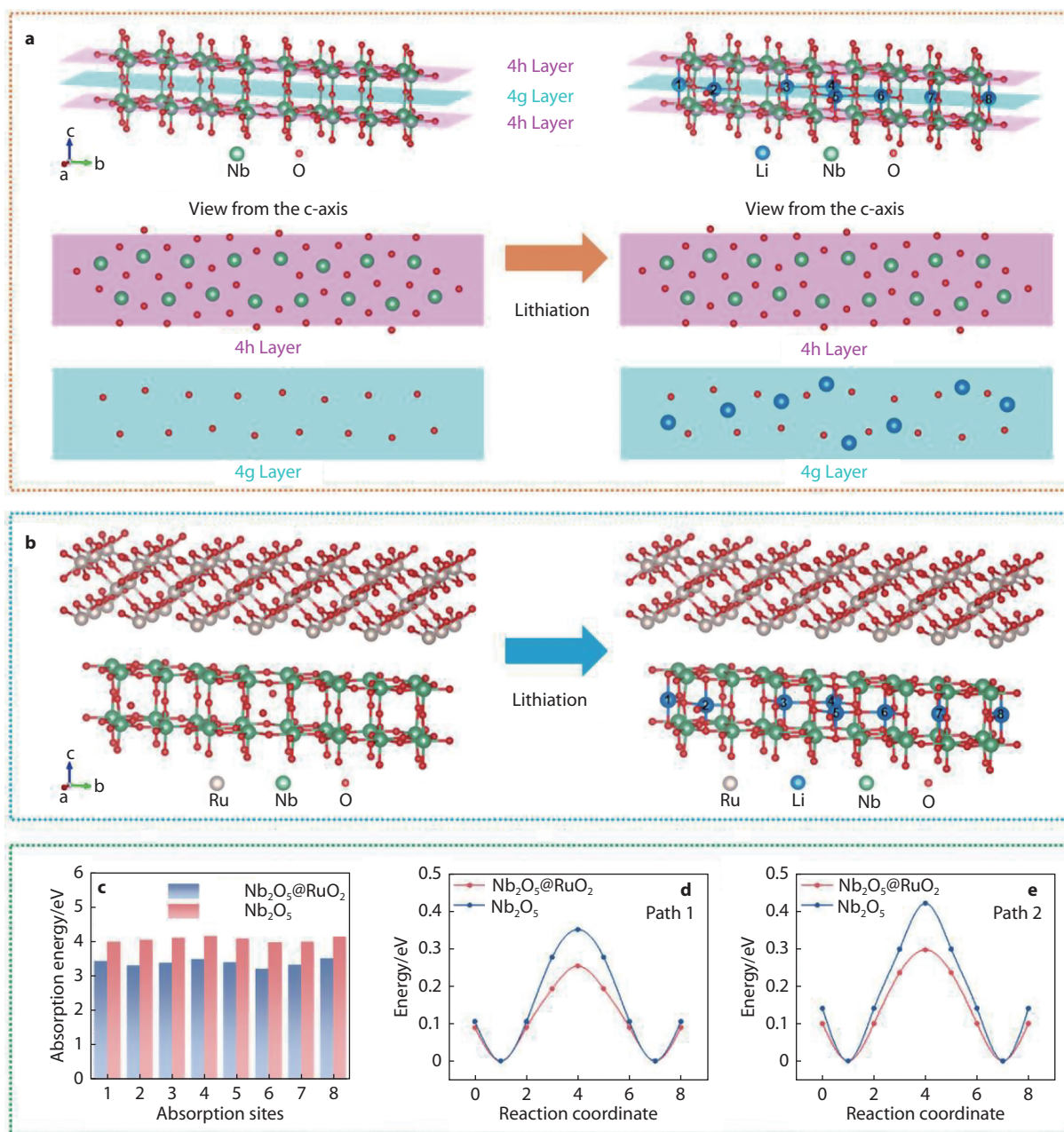


Fig. 6 **a**, Structure of the unlithiated model of Nb_2O_5 (left) and lithiated Nb_2O_5 (right). **b**, Structure of the unlithiated model of $\text{Nb}_2\text{O}_5@/\text{RuO}_2$ (left) and lithiated $\text{Nb}_2\text{O}_5@/\text{RuO}_2$ (right). **c**, The adsorption energies of Li ions on Nb_2O_5 and $\text{Nb}_2\text{O}_5@/\text{RuO}_2$ labeled in **a** and **b**. The Li ions migration barriers in Nb_2O_5 and $\text{Nb}_2\text{O}_5@/\text{RuO}_2$ along **d** path 1 and **e** path 2.

damental Research Funds for the Central Universities (WK2060140026), the China Postdoctoral Science Foundation (2020TQ0305, and 2021M693046), the “Transformational Technologies for Clean Energy and Demonstration” Strategic Priority Research Program of Chinese Academy of Sciences (Grant No. XDA21000000).

CONFLICT OF INTEREST

The authors declare no conflict of interest.

AUTHOR CONTRIBUTIONS

Hai Yang conceived and designed the project; Fuxiang He and Lixin He conducted the DFT calculations; Hai Yang, Jialong Shen, Zhihao Chen and Yu Yao performed the experiments; Hai Yang and Fuxiang He analyzed and discussed the experimental results and drafted the manuscript; all authors joined the discussion of data; Yan Yu proposed the research direction and guided the project. All authors had approved the final version.

■ REFERENCES

- B. Dunn, H. Kamath, J.-M. Tarascon, *Science*, 2011, 334, 928
- M. Armand, J.-M. Tarascon, *Nature*, 2008, 451, 652
- M. Li, J. Lu, Z. Chen, K. Amine, *Adv. Mater.*, 2018, 30, 1800561
- W. Cai, C. Yan, Y. X. Yao, L. Xu, X. R. Chen, J. Q. Huang, Q. Zhang, *Angew. Chem. Int. Ed.*, 2021, 60, 13007
- L. Ji, Z. Lin, M. Alcoutlabi, X. Zhang, *Energy Environ. Sci.*, 2011, 4, 2682
- L. Shen, E. Uchaker, X. Zhang, G. Cao, *Adv. Mater.*, 2012, 24, 6502
- L. Shen, S. Chen, J. Maier, Y. Yu, *Adv. Mater.*, 2017, 29, 1701571
- J.-T. Han, Y.-H. Huang, J. B. Goodenough, *Chem. Mater.*, 2011, 23, 2027
- H. Zhang, Y. Yang, H. Xu, L. Wang, X. Lu, X. He, *InfoMat*, 2022, 4, e12228
- M. M. Thackeray, K. Amine, *Nat. Energy*, 2021, 6, 683
- S. Li, X. Cao, C. N. Schmidt, Q. Xu, E. Uchaker, Y. Pei, G. Cao, *J. Mater. Chem. A*, 2016, 4, 4242
- Y. Zhang, C. Kang, W. Zhao, B. Sun, X. Xiao, H. Huo, Y. Ma, P. Zuo, S. Lou, G. Yin, *Energy Storage Mater.*, 2022, 47, 178
- V. Augustyn, J. Come, M. A. Lowe, J. W. Kim, P.-L. Taberna, S. H. Tolbert, H. D. Abruña, P. Simon, B. Dunn, *Nat. Mater.*, 2013, 12, 518
- Y. Zheng, Z. Yao, Z. Shadike, M. Lei, J. Liu, C. Li, *Adv. Funct. Mater.*, 2022, 32, 2107060
- F. Su, J. Qin, P. Das, F. Zhou, Z.-S. Wu, *Energy Environ. Sci.*, 2021, 14, 2269
- K. J. Woung, A. Veronica, D. Bruce, *Adv. Energy Mater.*, 2012, 2, 141
- J. Y. Cheong, C. Kim, J.-W. Jung, K. R. Yoon, S.-H. Cho, D.-Y. Youn, H.-Y. Jang, I.-D. Kim, *Small*, 2017, 13, 1603610
- H. Sun, L. Mei, J. Liang, Z. Zhao, C. Lee, H. Fei, M. Ding, J. Lau, M. Li, C. Wang, X. Xu, G. Hao, B. Papandrea, I. Shakir, B. Dunn, Y. Huang, X. Duan, *Science*, 2017, 356, 599
- C. Zhang, S. J. Kim, M. Ghidui, M.-Q. Zhao, M. W. Barsoum, V. Nicolosi, Y. Gogotsi, *Adv. Funct. Mater.*, 2016, 26, 4143
- Y. S. Hu, Y. G. Guo, R. Dominko, M. Gaberscek, J. Jamnik, J. Maier, *Adv. Mater.*, 2007, 19, 1963
- Y. Li, M. Bettge, J. Bareño, S. E. Trask, D. P. Abraham, *J. Electrochem. Soc.*, 2015, 162, 7049
- E. C. Gay, D. R. Vissers, F. J. Martino, K. E. Anderson, *J. Electrochem. Soc.*, 1976, 123, 1591
- M. Liu, C. Yan, Y. Zhang, *Sci. Rep.*, 2015, 5, 8326
- M. Wei, K. Wei, M. Ichihara, H. Zhou, *Electrochem. Commun.*, 2008, 10, 980
- M. M. Rahman, R. Abdul Rani, A. Z. Sadek, A. S. Zoofakar, M. R. Field, T. Ramireddy, K. Kalantar-zadeh, Y. Chen, *J. Mater. Chem. A*, 2013, 1, 11019
- S.-q. Guo, X. Zhang, Z. Zhou, G.-d. Gao, L. Liu, *J. Mater. Chem. A*, 2014, 2, 9236
- A. Le Viet, M. V. Reddy, R. Jose, B. V. R. Chowdari, S. Ramakrishna, *J. Phys. Chem. C*, 2010, 114, 664
- L. Kong, C. Zhang, S. Zhang, J. Wang, R. Cai, C. Lv, W. Qiao, L. Ling, D. Long, *J. Mater. Chem. A*, 2014, 2, 17962
- X. Wang, L. Ge, Z. Chen, V. Augustyn, X. Ma, G. Wang, B. Dunn, Y. Lu, *Adv. Energy Mater.*, 2011, 1, 1089
- Y. Tang, L. Yang, Y. Zhu, F. Zhang, H. Zhang, *J. Mater. Chem. A*, 2022, 10, 5620
- T. Li, K. Liu, G. Nam, M. G. Kim, Y. Ding, B. Zhao, Z. Luo, Z. Wang, W. Zhang, C. Zhao, J.-H. Wang, Y. Song, M. Liu, *Small*, 2022, 18, 2200972
- B. P. G., S. Bruno, T. Jean-Marie, *Angew. Chem. Int. Ed.*, 2008, 47, 2930
- L. Wang, X. Bi, S. Yang, *Adv. Mater.*, 2016, 28, 7672
- C. Chi, X. Xiuqiang, A. Babak, S. Asya, M. Taron, Z. Mengqiang, U. Patrick, M. Ling, J. Jianjun, G. Yury, *Angew. Chem. Int. Ed.*, 2018, 57, 1846
- K. Liao, X. Wang, Y. Sun, D. Tang, M. Han, P. He, X. Jiang, T. Zhang, H. Zhou, *Energy Environ. Sci.*, 2015, 8, 1992
- C. Seon-Jin, J. Ji-Soo, P. H. Jung, K. Il-Doo, *Adv. Funct. Mater.*, 2017, 27, 1606026
- S. Liang, L. Wen, S. Lin, J. Bi, P. Feng, X. Fu, L. Wu, *Angew. Chem. Int. Ed.*, 2014, 53, 2951
- P. Li, X. Liu, M. Chen, P. Lin, X. Ren, L. Lin, C. Yang, L. He, *Comp. Mater. Sci.*, 2016, 112, 503
- M. Ernzerhof, G. E. Scuseria, *J. Chem. Phys.*, 1999, 110, 5029
- M. Schlipf, F. Gygi, *Comput. Phys. Commun.*, 2015, 196, 36
- D. G. Smith, L. A. Burns, K. Patkowski, C. D. Sherrill, *J. Phys. Chem. Lett.*, 2016, 7, 2197
- D. Chen, J.-H. Wang, T.-F. Chou, B. Zhao, M. A. El-Sayed, M. Liu, *J. Am. Chem. Soc.*, 2017, 139, 7071
- H. Yang, R. Xu, Y. Gong, Y. Yao, L. Gu, Y. Yu, *Nano Energy*, 2018, 48, 448
- S. H. Jung, D. H. Kim, P. Bruner, H. Lee, H. J. Hah, S. K. Kim, Y. S. Jung, *Electrochim. Acta*, 2017, 232, 236
- E. Lim, J. Lee, C. Jo, Y. Mun, J. Chun, Y. Ye, J. Hwang, J. Lee, H. Kim, K. Kang, M.-H. Kim, K. C. Roh, K.-S. Ha, K. Kang, S. Yoon, *ACS Nano*, 2015, 9, 7497
- Z. Hu, Q. He, Z. Liu, X. Liu, M. Qin, B. Wen, W. Shi, Y. Zhao, Q. Li, L. Mai, *Sci. Bull.*, 2020, 65, 1154
- Y. G. Guo, Y. S. Hu, W. Sigle, J. Maier, *Adv. Mater.*, 2007, 19, 2087
- Y. Zhang, P. Chen, Q. Wang, Q. Wang, K. Zhu, K. Ye, G. Wang, D. Cao, J. Yan, Q. Zhang, *Adv. Energy Mater.*, 2021, 11, 2101712
- X. Wang, H. Li, H. Li, S. Lin, W. Ding, X. Zhu, Z. Sheng, H. Wang, X. Zhu, Y. Sun, *Adv. Funct. Mater.*, 2020, 30, 1910302
- K. E. Gregorczyk, A. C. Kozen, X. Chen, M. A. Schroeder, M. Noked, A. Cao, L. Hu, G. W. Rubloff, *ACS Nano*, 2015, 9, 464
- Z.-S. Wu, D.-W. Wang, W. Ren, J. Zhao, G. Zhou, F. Li, H.-M. Cheng, *Adv. Funct. Mater.*, 2010, 20, 3595
- R. M. Pittman, A. T. Bell, *J. Phys. Chem.*, 1993, 97, 12178
- L. Yang, Y. E. Zhu, J. Sheng, F. Li, B. Tang, Y. Zhang, Z. Zhou, *Small*, 2017, 13, 1702588
- C. Zhao, C. Yu, M. N. Banis, Q. Sun, M. Zhang, X. Li, Y. Liu, Y. Zhao, H. Huang, S. Li, X. Han, B. Xiao, Z. Song, R. Li, J. Qiu, X. Sun, *Nano Energy*, 2017, 34, 399
- T. Liu, J.-J. Xu, Q.-C. Liu, Z.-W. Chang, Y.-B. Yin, X.-Y. Yang, X.-B. Zhang, *Small*, 2017, 13, 1602952
- S. Fu, Q. Yu, Z. Liu, P. Hu, Q. Chen, S. Feng, L. Mai, L. Zhou, *J. Mater. Chem. A*, 2019, 7, 11234
- Q. Deng, M. Li, J. Wang, K. Jiang, Z. Hu, J. Chu, *Nanotechnology*, 2018, 29, 185401
- X. Wang, C. Yan, J. Yan, A. Sumboja, P. S. Lee, *Nano Energy*, 2015, 11, 765
- D. Cao, Z. Yao, J. Liu, J. Zhang, C. Li, *Energy Storage Mater.*, 2018, 11, 152
- M. Y. Song, N. R. Kim, H. J. Yoon, S. Y. Cho, H.-J. Jin, Y. S. Yun, *ACS Appl. Mater. Interfaces*, 2017, 9, 2267
- E. Lim, H. Kim, C. Jo, J. Chun, K. Ku, S. Kim, H. I. Lee, I.-S. Nam, S. Yoon, K. Kang, J. Lee, *ACS Nano*, 2014, 8, 8968
- B. Deng, T. Lei, W. Zhu, L. Xiao, J. Liu, *Adv. Funct. Mater.*, 2018, 28, 1704330
- K. Brezesinski, J. Wang, J. Haetge, C. Reitz, S. O. Steinmueller, S. H.

- Tolbert, B. M. Smarsly, B. Dunn, T. Brezesinski, *J. Am. Chem. Soc.*, 2010, 132, 6982
64. T. Brezesinski, J. Wang, S. H. Tolbert, B. Dunn, *Nat. Mater.*, 2010, 9, 146
65. D. Chao, P. Liang, Z. Chen, L. Bai, H. Shen, X. Liu, X. Xia, Y. Zhao, S. V. Savilov, J. Lin, Z. X. Shen, *ACS Nano*, 2016, 10, 10211
66. D. Chao, C. Zhu, P. Yang, X. Xia, J. Liu, J. Wang, X. Fan, S. V. Savilov, J. Lin, H. J. Fan, Z. X. Shen, *Nat. Commun.*, 2016, 7, 12122
67. H. J. Liang, Z. Y. Gu, X. X. Zhao, J. Z. Guo, J. L. Yang, W. H. Li, B. Li, Z. M. Liu, W. L. Li, X. L. Wu, *Angew. Chem. Int. Ed.*, 2021, 60, 26837
68. Z.-Y. Gu, J.-Z. Guo, Z.-H. Sun, X.-X. Zhao, X.-T. Wang, H.-J. Liang, X.-L. Wu, Y. Liu, *Cell Rep. Phys. Sci.*, 2021, 2, 100665
69. Q. Deng, Y. Fu, C. Zhu, Y. Yu, *Small*, 2019, 15, 1804884
70. G. Henkelman, B. P. Uberuaga, H. Jónsson, *J. Chem. Phys.*, 2000, 113, 9901
71. A. Heyden, A. T. Bell, F. J. Keil, *J. Chem. Phys.*, 2005, 123, 224101



©2023 The Authors. *Energy Lab* is published by Lab Academic Press. This is an open access article under the terms of the Creative Commons Attribution License, which permits use, distribution and reproduction in any medium, provided the original work is properly cited.